

Effective Window Function for Lagrangian Halos

Kwan Chuen Chan^{(1,2),*} Ravi K. Sheth⁽³⁾, and Román Scoccimarro⁽⁴⁾

¹ *Département de Physique Théorique and Center for Astroparticle Physics, Université de Genève, 24 quai Ernest Ansermet, CH-1211 Genève 4, Switzerland*

² *Institut de Ciències de l'Espai, IEEC-CSIC, Campus UAB, Carrer de Can Magrans, s/n, 08193 Bellaterra, Barcelona, Spain*

³ *Center for Particle Cosmology, University of Pennsylvania, 209 S. 33rd St., PA 19104, Philadelphia, USA and*

⁴ *Center for Cosmology and Particle Physics, Department of Physics, New York University, NY 10003, New York, USA*

(Dated: August 29, 2022)

The window function for the Lagrangian halos is often assumed to be a top hat function. We measure the profile of the Lagrangian halo directly and find that it is more extended than a top hat but less diffuse than a Gaussian. We find that the Lagrangian profile can be described well by an effective window composed of a product of a top hat and a Gaussian window in Fourier space. We also check that the same effective window function together with the scale-dependent excursion set bias parameters fits the Lagrangian cross bias parameter in Fourier space well up to $kR_{\text{Lag}} \sim 10$, where R_{Lag} is the Lagrangian size of the halo. The effective window is simple in Fourier space, and there is also an analytic form in real space, thus there is little work in converting from the usual top hat window to the effective window. With the effective window function, all the spectral moments of the power spectrum are finite, thus we have a unified treatment for computing the spectral moments in peak and excursion set peak theories. When the effective window function is used, the resultant excursion set peak mass function is significantly lower compared to that obtained from the mixed window function approach, and hence this causes the excursion set peak mass function to be appreciably lower than the simulation results for halos of mass $\lesssim 10^{14} M_{\odot} h^{-1}$. We can interpret this deficit as that only part of the low to medium mass halos can arise from peaks.

I. INTRODUCTION

In excursion set theories [1] and peak models [2–7], the Lagrangian halos are modeled by smoothing the dark matter density field with a window function. The window function can be interpreted as a selection function which selects a fraction of the local dark matter density that would form the Eulerian halo later on. Thus to define halos, one expects the window function to be localized in real space. This window function is often assumed to be a top hat partly because of the spherical collapse model. Under the spherical collapse model [8–10], the evolution of a spherical shell is governed by the mean overdensity inside the spherical shell. Since only the mean density contrast matters, one may for convenience assume a uniform top hat perturbation. The top hat assumption has the added simplicity that the top hat profile is maintained during collapse perhaps up to violent relaxation [11]. Thus top hat windows are often invoked in theoretical modeling of the Lagrangian halos due to its simplicity.

Probably no one expects that the top hat assumption to hold exactly. As the measurements and theoretical predictions become more precise, we have to check how accurate this assumption is and how much systematics that it may cause. There are elaborate models such as the peak model [2–7] and the excursion set peaks model

[12–15] that predict the clustering of the Lagrangian halos. In these models the spectral moments of the power spectrum are essential, however, high order spectral moments are ill-defined for top hat window due to its slow decay in Fourier space. To alleviate this problem, one usually takes a hybrid approach by computing the zeroth moment with a top hat, while higher order ones with a Gaussian window, e.g. [14–16]. It is more satisfactory if one can find a unified treatment for all the moments. Another important reason for modeling the window function well is that these models predict the bias parameters to be scale-dependent. While they predict the scale-dependent bias parameters in precise form, the window function is left unconstrained. As both the window function and the bias parameters give rise to scale-dependence, one must model both of them well in order to disentangle their scale-dependent contributions.

In this paper, we will concentrate on the window function of the Lagrangian halos. There are scattered hints from previous numerical works that the Lagrangian halos is more extended than a top hat [17–21], we will quantify the profile of the Lagrangian halos here. We shall show that the Lagrangian halo window function is neither a top hat nor a Gaussian, instead it is well described by a product of a top hat and a Gaussian in Fourier space (see also [22, 23]). This paper is organized as follows. In Sec. II, we reconstruct the Lagrangian halo profile from simulation and then we propose a parametrization to fit the profile. We measure the cross power spectrum between the dark matter and the Lagrangian halo in Sec. III. We will show that the same effective function together with the excu-

* chan@ice.cat

sion set bias parameters enable us to fit the the cross bias parameter well. After checking that the effective window works for both real space and Fourier space measurements, we check how the excursion set mass function changes when the effective window is used to compute the spectral moments in Sec. IV. In Sec. V, we check if the halo model formalism can describe the Lagrangian cross power spectrum. We conclude in Sec. VI. The linking length dependence of the Lagrangian halo profile is checked in Appendix A. The excursion set peak mass function is reviewed and extended to general window function in Appendix B. We review the derivation of the cross power spectrum in the halo model formalism in Appendix C.

II. LAGRANGIAN HALO PROFILE

In the Lagrangian models for halos, we postulate that the final Eulerian halos are seeded by the proto-halos in the Lagrangian space. These Lagrangian halos evolve to form the halos in the Eulerian space. Thus the physics of the Eulerian halos may be understood by studying the proto-halos. The statistics in the Lagrangian space is much simpler than that in the Eulerian space because the initial field is Gaussian if no primordial non-Gaussianity is assumed.

To study the halos in Lagrangian space numerically, we construct the Lagrangian halos as follows. From the Eulerian halos at some redshift z , typically $z = 0$ and 0.97 in this paper, we trace back the constituent particles in each halo to the initial redshift z_* . The center of mass of the Lagrangian halo is estimated using the center of mass of the constituent particles in the Lagrangian space.

In this work, we shall use two sets of simulations in the LasDamas project, denoted by Oriana and Carmen respectively. In both simulations, the same flat Λ CDM model with the cosmological parameters, $\Omega_m = 0.25$, $\Omega_\Lambda = 0.75$ and $\sigma_8 = 0.8$ are adopted. The transfer function is output from CMBFAST [24]. The initial conditions are Gaussian with spectral index being 1. The initial particle displacement fields are set using 2LPT [25] at $z_* = 49$. The simulations are evolved using the public code Gadget2 [26]. In the Oriana simulations, there are 1280^3 particles in a cubic box of size $2400 \text{ Mpc } h^{-1}$. There are 1120^3 particles in a box of size $1000 \text{ Mpc } h^{-1}$ for the Carmen simulations. Thus in Oriana and Carmen simulations, each particle carries a mass of 4.57×10^{11} and $4.94 \times 10^{10} M_\odot h^{-1}$ respectively. We shall average over 5 realizations for Oriana, and 7 for Carmen. The Eulerian halos are identified using the Friend-Of-Friend algorithm [27]. Unless otherwise stated, we use FOF halos with linking length $b = 0.156$. Only in the Appendix A, where we compare the profile of the Lagrangian halos obtained with $b = 0.156$ and $b = 0.2$, we use halos with $b = 0.2$ as well. The halo catalogs are constructed at $z = 0.97$ and 0 . In order to resolve the halo profile well, we consider halos with at least 150 particles. We bin the halos into

thin narrow mass bins of width $\Delta \ln M = 0.157$.

A. Reconstructing the Lagrangian window function from simulation

There are several requirements that we expect the window function W to satisfy. To be able to define a halo in Lagrangian space, we expect it to be compact and reasonably well localized in real space. Also we have $W(\mathbf{x}) \geq 0$ and

$$\int d^3x W(x) = 1. \quad (1)$$

We will further impose the spherical symmetry requirement. The usual top hat and Gaussian window function clearly satisfy these conditions. With these conditions, we can reconstruct the window function from the Lagrangian halo profile.

Suppose the halo center is located at the origin, the total number of particles in this halo, N is given by

$$N = \int d^3x n_h(\mathbf{x}), \quad (2)$$

where n_h is the number density of the dark matter particles belonging to this Lagrangian halo. Let the probability that a dark matter particle at a distance r is incorporated into the Lagrangian halo be p_h , then we can write N as

$$N = \int dr 4\pi r^2 p_h(r) n_m(r), \quad (3)$$

where n_m is the number density of the underlying dark matter density, which is different from the mean dark matter number density \bar{n}_m if the clustering is not negligible. To construct the Lagrangian halo profile, we will remove the clustering effect either by tracing the particles back to their initial grid points or by modeling the clustering and then dividing it out. We will show results from both approaches. As we assume that the clustering effects will be removed by either means, we can safely take n_m to be \bar{n}_m here.

Although the Lagrangian halo profile is not top hat, still we find it convenient to define the Lagrangian radius R_{Lag} as

$$N = \frac{4\pi}{3} \bar{n}_m R_{\text{Lag}}^3. \quad (4)$$

Therefore by comparing with Eq. 1, we can extract the window function as

$$W(r) = \frac{3p_h(r)}{4\pi R_{\text{Lag}}^3}. \quad (5)$$

The probability $p_h(r)$ can be estimated by the ratio $n_h(r)/n_m(r)$, where $n_h(r)$ is the number density of the particles belonging to the Lagrangian halo. The results

are shown in Fig. 1. To compute $n_h(r)$, for each Lagrangian halo, we bin all the particles at the grid position belonging to the Lagrangian halo into spherical shells about the center of mass of the halo, and we then compute the number density of the shells. The spherically averaged number density is further averaged over all the halos in the same mass bin. We carry out the same procedure for all the particles around the halo center to compute $n_m(r)$. We emphasize that in both cases we have used the particles traced back to the initial grid points, not the displaced position in the displaced field to get rid of the effects of the clustering so that we can replace n_m by \bar{n}_m in Eq. 3. This method is also used in [22].

In Fig. 1, we have shown the measurements from both Carmen and Oriana simulations with Lagrangian halos obtained from Eulerian halos at $z = 0.97$ and 0 respectively. The results from $z = 0.97$ and $z = 0$ are very similar. To absorb most of the mass dependence, the radius is normalized with respect to R_{Lag} . We find that in this normalized variable, the results from halos spanning two orders of magnitude in mass follow a very similar profile. However, there is small residual mass dependence left. The less massive halos are slightly more diffuse than the more massive ones.

From Fig. 1, we see that the profile drops sharply at $r/R_{\text{Lag}} \sim 1$, but it is more smooth than a top hat window. It is also more localized in real space than a Gaussian window. It is noteworthy that even for $r/R_{\text{Lag}} \lesssim 0.5$, p_h is still a few per cent less than 1. This means that even in the Lagrangian patch close to the center of mass of the Lagrangian halo, on average a small fraction of dark matter particles still are not incorporated into the final Eulerian halo.

The results shown in Fig. 1 is similar to Fig. 3 in [22] where the measurement of p_h was presented. They also pointed out that the Lagrangian window is more diffuse than a top hat but more compact than a Gaussian. However, the authors in [22] considered the scale-free power spectrum, here we use the realistic power spectrum. More importantly we also propose the parametrization Eq. 9 to fit the profile. We also note that we have considered all the halos without further screening. The Lagrangian halo may consist of more than one lump of matter. If we use only the main lump in the Lagrangian halo as in [19], the resultant p_h near the center would be closer to 1 than what we have obtained.

B. A model for Lagrangian halo window function

Suppose in some spherical Lagrangian patch, if all the particles within this patch end up in the Eulerian halo, the window function is given by a top hat. Realistically, we expect that some particles in this patch with velocity higher than the escape velocity will get out of the patch while some outside the patch will get in. These motivate us to consider a composite window consisting of a top hat

being smoothed by a Gaussian. If the scale of the top hat is given by the Lagrangian size R_{Lag} then it remains to fix the scale of the Gaussian smoothing window. We find that when the smoothing scale is close to the Eulerian scale of the halo the window gives a good description of the numerical data. Of course, if we have assumed other smoothing window other than a Gaussian, the smoothing scale will be slightly different.

In Fourier space, we propose to use the effective window function

$$W_{\text{eff}}(kR_{\text{Lag}}) = W_{\text{TH}}(kR_{\text{Lag}})W_{\text{G}}\left(\frac{\sqrt{f}kR_{\text{Lag}}}{5}\right), \quad (6)$$

where W_{TH} and W_{G} denote the top hat and Gaussian window function respectively

$$W_{\text{TH}}(x) = \frac{3}{x^3}(\sin x - x \cos x), \quad (7)$$

$$W_{\text{G}}(x) = e^{-\frac{x^2}{2}}. \quad (8)$$

We have introduced the parameter f so that the smoothing scale can vary. By an inverse Fourier transform, we get the window in real space

$$W_{\text{eff}}(r) = \frac{3}{40\pi^2 r R_{\text{Lag}}^3} \left\{ \sqrt{2\pi} f R_{\text{Lag}} (e^{-x_+^2} - e^{-x_-^2}) - 5\pi [R_{\text{Lag}} \text{sign}(x_-) + |r - R_{\text{Lag}}|] \text{erf}(|x_-|) + 5\pi r \text{erf}(x_+) \right\}, \quad (9)$$

where

$$x_+ = \frac{5(r + R_{\text{Lag}})}{\sqrt{2f}R_{\text{Lag}}}, \quad x_- = \frac{5(r - R_{\text{Lag}})}{\sqrt{2f}R_{\text{Lag}}}, \quad (10)$$

and sign and erf denote the sign function and error function respectively.

We also show the best fit using the window function Eq. 9 in Fig. 1. To be general we allow additional fitting parameters to vary. More precisely, we consider the model

$$p_h(r) = \frac{4\pi A R_{\text{Lag}}^3}{3} W_{\text{eff}}(r; f, R), \quad (11)$$

and regard R , A and f as free parameters. We have replaced R_{Lag} in Eq. 9 by a free parameter R . Overall, we find that this model yields a good fit to the Lagrangian profile for the numerical profile. However, we also note that the profile model tends to be slightly more concentrated than the numerical result.

We plot the resultant best fit parameters in Fig. 2. We expect R/R_{Lag} and A to be close to 1. Indeed from Fig. 2, we find that the best-fit R/R_{Lag} is within 1% from 1. The best-fit A is a few per cents below 1, resulting from the fact that p_h is a few per cents below 1 even for small r . On the other hand, the deviation of f from 1 is larger than 50% at the end $\nu \sim 1.5$, but it decreases to the value close 1 at $\nu \sim 3.5$.

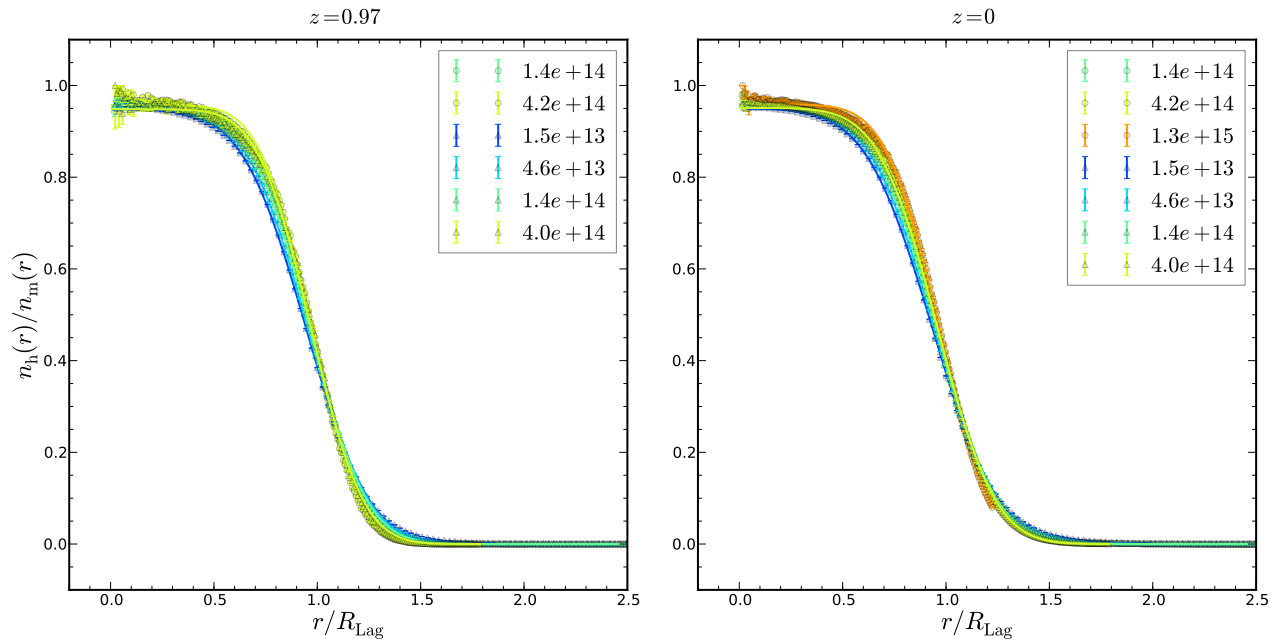


FIG. 1. The estimator n_h/n_m for p_h is obtained using data from Oriana (circular data points) and Carmen (triangular data points) simulations for a suite of halo mass shown in the legend (in unit of $M_\odot h^{-1}$). The best fit using Eq. 9 is also shown (solid line, the same color as the data points for the same mass group). The model fits the numerical window well.

C. Reconstructing the Lagrangian window with clustering correction

We now discuss the other method which use the displaced particles to estimate p_h . As we mentioned earlier, when the displaced particles instead of the particles traced back to the grid points are used, we cannot replace n_m by \bar{n}_m . Due to the presence of the halo at the origin, n_m is enhanced by a factor as

$$n_m(r) = \bar{n}_m[1 + \xi_c(r)], \quad (12)$$

where ξ_c is the cross correlation function between halo and matter. We can either measure ξ_c directly or model it. To model ξ_c we use the bias model Eq. 17 given below together with the bias parameters computed from the peak model [14] to obtain the cross power spectrum. Then ξ_c follows after an inverse Fourier transform. As in this paper, we focus on the window function, we will present the details of the model and the comparison with numerical measurements elsewhere [28]. We find that the model we adopted describes the simulation data well. Hence we will use ξ_c obtained from theory here. In Fig. 3, we compare the measurement n_h^d/\bar{n}_m and $n_h^d/\bar{n}_m/(1+\xi_c)$, where the superscript d in n_h^d emphasizes that it is estimated using the displaced particle distribution. We have used the Lagrangian halos at $z=0$ from Carmen simulation in this plot. The clustering correction is mainly important for $r \lesssim R_{\text{Lag}}$, while for larger r , $\xi_c \ll 1$. Due to the clustering enhancement, n_h^d/\bar{n}_m exceeds 1 for $r/R_{\text{Lag}} \lesssim 0.5$. After the correction, we find that the

results agree with those from the previous method very well (right panel of Fig. 1). This method is interesting in its own right. We are able to correct the clustering effect is a non-trivial consistency check of the formalism.

D. Lagrangian halo profile and spherical collapse

We find that contrary to the usual top hat assumption, the Lagrangian halo profile is more extended. We now contrast the Lagrangian halo profile obtained with the spherical collapse (SC) picture [8–10]. In SC the fate of a spherical patch of size r is determined by the mean overdensity inside r . If the average overdensity is higher than certain threshold, the patch collapses, while it expands otherwise.

From the halo profile, we can compute the mean overdensity inside r as

$$\bar{\delta}_h(r) = \frac{3 \int_0^r dr' r'^2 n_h(r')}{r^3 \bar{n}_m} - 1. \quad (13)$$

In Fig. 4, we have plotted the average overdensity inside radius r obtained from the numerical profile in Fig. 1. For clarity, we do not show the average obtained from the best-fit profile as they are very similar to the numerical results. We have also plotted the mean overdensity expected from SC for it to collapse at $z=0$. It is obtained by extrapolating δ_c to $z_* = 49$ using the linear growth factor. We find that the average overdensity is less than

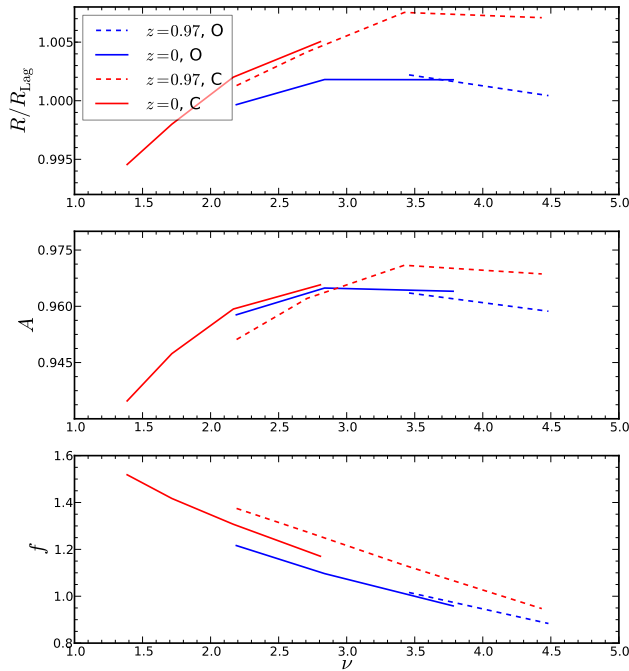


FIG. 2. The best-fit parameters R , A and f for the Lagrangian halo profile. The best fit to the data from Oriana (blue) and Carmen (red) at $z = 0.97$ (dashed) and 0 (solid) are shown.

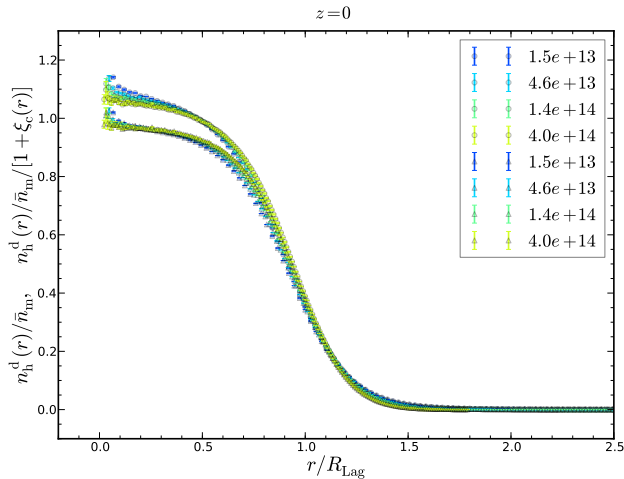


FIG. 3. The ratio n_h^d/\bar{n}_m obtained using displaced particles at the initial redshift $z_* = 49$ (circles, the upper set of curves) and the one with clustering effect corrected $n_h/\bar{n}_m/(1 + \xi_c)$ (triangles, the lower set). The Lagrangian halos at $z = 0$ from Carmen simulation are used.

the collapse threshold. This implies that generically we cannot obtain realistic halos by simply considering an isolated Lagrangian patch collapsing spherically. This is because the application of the SC model suggests that

the region with average overdensity less than the threshold would expand rather than collapse. This is however consistent with the hierarchical structure formation, in which halos undergo accretion and merger to form the final Eulerian halo. The Lagrangian halo can consist of various Lagrangian sub-patches, rather than a single isolated one. Because of the wide spread of the Lagrangian particles, the mean overdensity is even less than 0.

It is important to note that the Lagrangian halo profile is not the quantity that directly related to the SC. Although in SC, all the particles within a shell whose mean overdensity exceeds the threshold will end up in the final Eulerian halo. However, that is a consequence of the model, the input of SC is only the fluctuations around the origin, there is no reference to whether they will form the final halo or not. Furthermore it does not mean that at the position of the Lagrangian halo, the overdensity is lower than average because to construct the profile we only use the particles ending up in the final Eulerian halo. To measure the overdensity at the position of the Lagrangian halo, we should instead use *all* the particles in the dark matter field. If so we will get n_h which is enhanced by ξ_c and it is indeed higher than the SC collapse threshold (see [28]).

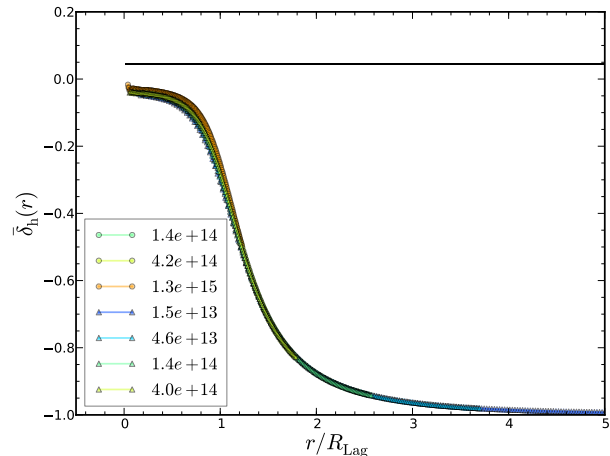


FIG. 4. The mean density profile inside radius r , obtained using the Lagrangian profile at $z = 0$. The data from Oriana (circles) and Carmen (triangles) are shown. The SC threshold at $z_* = 49$ is plotted for comparison (black line).

III. LAGRANGIAN CROSS BIAS PARAMETER

The excursion set theory naturally predicts the cross correlation between the halo center and the dark matter. We shall focus on the cross power spectrum in this section and will not discuss the auto-power spectrum. Another advantage of the cross power spectrum is that it is proportional to the linear dark matter power spectrum

[29]. We can compute the cross power spectrum between density contrast of the Lagrangian halo, δ_h , and that of the dark matter at the initial time, δ_m ,

$$\langle \delta_h(\mathbf{k}_1) \delta_m(\mathbf{k}_2) \rangle = (2\pi)^3 P_c(k_1) \delta_D(\mathbf{k}_{12}), \quad (14)$$

where δ_D is the Dirac delta function. Similarly, the Lagrangian matter power spectrum is defined as

$$\langle \delta_m(\mathbf{k}_1) \delta_m(\mathbf{k}_2) \rangle = (2\pi)^3 P_m(k_1) \delta_D(\mathbf{k}_{12}). \quad (15)$$

Using P_c and P_m , we can define the Lagrangian cross bias parameter

$$b_c^L(k, z) = \frac{D(z_*)}{D(0)} \left[\frac{P_c(k)}{P_m(k)} - 1 \right], \quad (16)$$

where we extrapolate the Lagrangian bias parameter to $z = 0$ using the linear growth factor D . We have included the term -1 because of finite initial redshift of the simulation, see e.g. [30].

In Fig. 5, we show the Lagrangian bias parameters b_c^L obtained from halos at $z = 0.97$ and 0 for a suite of halo masses. To absorb some of the mass dependence, we have plotted b_c^L against kR_{Lag} . We have used Lagrangian halo data at $z = 0.97$ and 0 from both Oriana and Carmen simulations. Again b_c^L from halos of different masses and redshifts exhibit similar features. For $kR_{\text{Lag}} \lesssim 1$, they approach a constant, and there is a peak for $kR_{\text{Lag}} \sim$ a few. Then b_c^L drops sharply, but it exhibits oscillatory features for larger kR_{Lag} with diminishing amplitudes.

A simple model for the Lagrangian cross bias b_c^L is

$$b_{\text{eff}}(k) = b_{10} W_{\text{eff}}(k) + 2b_{01} \frac{dW_{\text{eff}}(k)}{d \ln s_0}, \quad (17)$$

In general, the spectral moments of the power spectrum s_j , or σ_j^2 is defined as

$$s_j = \sigma_j^2 = \int \frac{dk}{k} \frac{4\pi k^3}{(2\pi)^3} k^{2j} P_m(k, 0) W_{\text{eff}}^2(kR), \quad (18)$$

with $P_m(k, 0)$ being the linear dark matter power spectrum extrapolated to $z = 0$. The bias parameters b_{10} and b_{01} are of the same dimension. These two bias parameters arise from two constraints on the excursion set trajectories. The b_{10} -term is due to the threshold constraint that whenever the trajectory crosses it at s_0 , it is interpreted as the site of halo formation with halo mass associated with s_0 . The b_{01} -term comes from the first crossing constraint that the trajectory has to satisfy a further condition that it does not cross the threshold at any $s'_0 < s_0$. The b_{01} -term in Eq. 17 is scale-dependent arising from the derivative of the window function. Therefore one must model the window function accurately in order to extract the scale-dependent bias. Eq. 17 is similar to that in [31] except we have adopted the effective window W_{eff} . There is a more refined excursion set peak model [14], in which a further condition that the point is a peak is imposed. The first crossing constraint is more fundamental as it solves the cloud-in-cloud problem and gives

the correct mass function in the excursion set theory. The additional term due to the curvature constraint is highly degenerate with the b_{01} -term for the cross power spectrum. Thus only including the b_{01} -term captures most of the scale dependence already. We shall discuss more on the excursion set peak model in [28], while we will focus on the model Eq. 17 here.

In peak and excursion set peak models, one must compute high order moments of the power spectrum beside s_0 . For example, although in Eq. 17 we only need s_0 , the theoretical prediction for b_{10} and b_{01} from peak model [5, 14] involves higher order moments as well. In the usual treatments, e.g. [14–16], in which one uses W_{TH} to compute s_0 , but for higher order spectral moments one opts to use W_G as W_{TH} leads to divergence. Although W_{eff} is more localized in real space than a Gaussian window, and yet all the spectral moments are finite because of its Gaussian component. Thus we can have a unified treatment for all the moments when W_{eff} is used. In this paper, unless otherwise stated, we shall compute the moments using W_{eff} . In a similar vein, we discuss the excursion set peak mass function when the effective window function is used in Sec. IV.

The bias model Eq. 17 typically can fit b_c^L up to the peak without much sensitivity to the window function adopted. However, to get the oscillatory features in the larger kR_{Lag} region right, an accurate window is required. If the top hat window is used, it will exhibit too much oscillations for $kR_{\text{Lag}} \gtrsim 3$. In the previous works [18, 20], Gaussian window was adopted and the first peak can be fitted well, but the oscillatory features for larger kR_{Lag} are missed. Here again we see that the effective window should be in between a top hat and a Gaussian window. We plot the best fit using Eq. 17 in Fig. 5 as well. We have treated b_{10} , b_{01} and R as free parameters in the fitting. We have set $f = 1$ in W_{eff} . In the fitting, we first determine b_{10} by fitting to the low k constant part, more precisely, $kR_{\text{Lag}} < 0.15$. We can do this because at low k , W_{eff} approaches 1 while the scale dependent term vanishes. We then keep the best-fit b_{10} fixed and fit the remaining parameters, b_{01} and R . Overall, b_{eff} fits the features of b_c^L from simulations well. As the focus of this paper is on the Lagrangian window, we shall not describe the best-fit bias parameters in details here. We will present the details of the bias measurements and their implications elsewhere [28]. However, we note that R is roughly within 10% from R_{Lag} . This means that both the halo profile in real space and the cross bias parameter in Fourier space require the same W_{eff} . This is an important consistency check of the model.

IV. EXCURSION SET PEAK MASS FUNCTION USING THE EFFECTIVE WINDOW

Unlike the excursion set approach [1], the peak model [2] only takes one particular scale into account. The excursion set approach assumes that the halo abundance

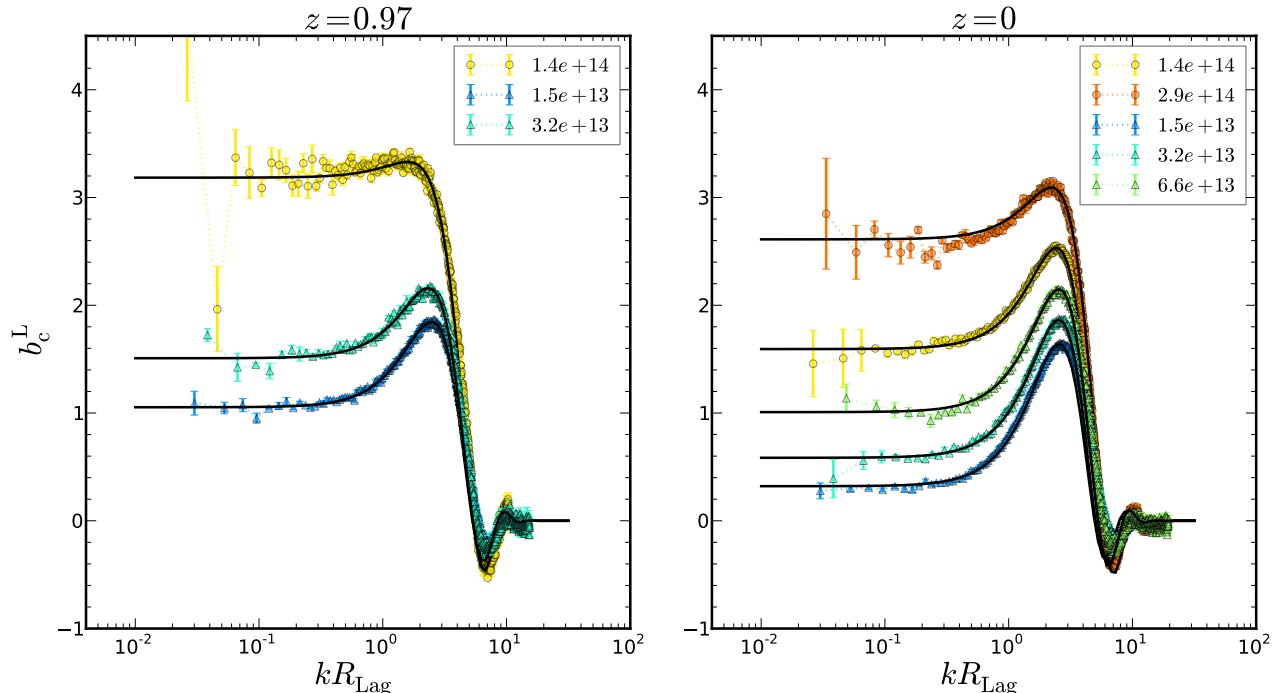


FIG. 5. The Lagrangian cross bias parameter b_c^L for Lagrangian halos constructed from the Eulerian halos at $z = 0.97$ (left panel) and $z = 0$ (right panel). The mass of the halos are shown in the legend (in unit of $M_\odot h^{-1}$). The data are from Oriana (circle) and Carmen (triangle) simulations. The best-fit using Eq. 17 is also plotted (solid, black).

can be obtained by averaging over random points, while in peak model, the average is taken over the peak positions only. Refs. [12–14] incorporated the first crossing constraint, which is crucial in the excursion set formalism, into the peak model. Hence the resultant model is dubbed excursion set peak (ESP). The spectral moments (Eq. 18) play an important role in the ESP model, and s_j depends on the window function used, in this section we shall check how the ESP mass function changes when the effective window is used. In Appendix B, we review the derivations of the ESP mass function in details. In particular, in [12–14] the Gaussian window function was assumed, we will generalize the ESP mass function to arbitrary window function.

We shall follow the prescription in [14], in which the mass dependence of the barrier and the scatter around the barrier are important ingredients. The barrier is modeled by

$$B(s_0) = \delta_c + \epsilon\sqrt{s_0}, \quad (19)$$

where the square-root model is to describe the scale-dependence of the barrier and ϵ controls the scatter around the barrier (Note that our ϵ is β in [14]). The ESP multiplicity function f_{esp} is obtained by averaging over the scatter

$$f_{\text{esp}}(\nu) = \int d\epsilon f_{\text{esp}}(\nu|\epsilon)p(\epsilon). \quad (20)$$

Ref. [14] followed [32] to use log-normal distribution for $p(\epsilon) = 0.5$ with $\langle\epsilon\rangle$ and $\text{Var}(\epsilon) = 0.25$. As our aim here is to check the effect of the window function, we shall do the same.

For the Gaussian window, the conditional ESP multiplicity function is given by [14]

$$f_{\text{esp}}^G(\nu|\epsilon) = \frac{V}{V_*} \frac{e^{-(\nu+\epsilon)^2/2}}{\sqrt{2\pi}} \frac{1}{\gamma\nu} \int_{\epsilon\gamma}^{\infty} dx (x - \epsilon\gamma) \times f(x)p_G(x;\nu\gamma, 1 - \gamma^2), \quad (21)$$

where γ is the correlation coefficient defined in Eq. B22. The explicit form of $f(x)$ is given in Eq. B43 and the volumes V and V_* are defined in Eq. B46. Note that compare to [14] we have neglected the shift in mean of p_G due to the scatter, and we have checked that its effects are small.

As we mentioned, the ESP mass function in the literature explicitly assumes the Gaussian window. We derive the ESP mass function for arbitrary window function in Appendix B. The final f_{esp} can be written as

$$f_{\text{esp}}(\nu|\epsilon) = \frac{V}{V_*} \frac{e^{-(\nu+\epsilon)^2/2}}{\sqrt{2\pi}} \frac{1}{\alpha\nu} E(\nu, \alpha, \beta, \gamma), \quad (22)$$

where E is given by Eq. B50 and the results depend on additional cross correlation coefficients α and β (Eq. B20 and B21). When Gaussian window is used, α is the same

as γ . The function E can be regarded as a generalization of the integral in Eq. 21.

From f_{esp} , we can derive the halo mass function as usual

$$\frac{dn}{d\ln M} = \frac{\rho_m}{M} \frac{d\ln \nu}{d\ln M} \nu f_{\text{esp}}(\nu). \quad (23)$$

The window function dependence comes from the spectral moments and also the precise form of f_{esp} . We shall consider three cases. In the first case, we follow the prescription in [14] to compute $f_{\text{esp}}^{\text{G}}$ (Eq. 21) using mixed windows. We shall abbreviate it by W_{mix} . In the second case, $f_{\text{esp}}^{\text{G}}$ is used, but the moments are computed using W_{eff} only. We denote this case by “partial W_{eff} ”. In the third scenario, we use f_{esp} in Eq. 22 and the moments computed with W_{eff} . We abbreviate this case by “full W_{eff} ”. This can help us to find out whether the spectral moments or the functional form of f_{esp} contribute most significantly.

When the effective window is used, we simply compute all the spectral moments using W_{eff} . For the case with mixed window, it is more complicated and we shall follow [14], in which s_0 is computed with top hat window and s_2 with Gaussian window. We map R_{Lag} to the corresponding Gaussian smoothing scale R_{G} by matching the k^2 coefficient of the window function in Fourier space, i.e.

$$R_{\text{G}} = \frac{R_{\text{Lag}}}{\sqrt{5}}. \quad (24)$$

Although in [14] another mapping criterion $\langle \delta_{\text{G}} | \delta_{\text{TH}} \rangle = \delta_{\text{TH}}$ was adopted instead, the result is very similar to Eq. 24. For V_* , s_1 is computed using the Gaussian window only, whereas for γ , s_1 is computed using mixed window, both top hat and Gaussian.

In Fig. 6 we plot f_{esp} evaluated at $z = 0$ obtained using the three different scenarios. We find that in the low mass region of this plot, such as $M \sim 10^{12} M_{\odot} h^{-1}$, f_{esp} obtained from the effective window is lower than that from the mixed window by almost a factor of 2 or more. The full W_{eff} result is even lower than the partial W_{eff} case. While for larger mass, $M \gtrsim 10^{15} M_{\odot} h^{-1}$, the difference between the mixed window and the full W_{eff} becomes quite small. One of the main difference between the mixed window case and the effective window case comes from the factor $(V/V_*)/(\gamma\nu)$ as it is computed with the spectral moments. For example, we find that at $M = 2 \times 10^{13} M_{\odot} h^{-1}$, compared to the value obtained from the mixed window it is about 0.53 of the mixed window value for the partial W_{eff} and 0.59 for the full W_{eff} case. The overall mass dependence of this factor is relatively weak. Thus the mass dependence we see in Fig. 6 mainly comes from the difference between the integral in Eq. 21 and E in Eq. 22.

In [14], the ESP mass function was found to yield good agreement with the numerical results (within 5%) using mixed window in the mass range from 10^{11} to $2 \times 10^{14} M_{\odot} h^{-1}$ (or from $\nu = 0.6$ to 2.2). However Fig. 6 suggests that when the effective window is used,

f_{esp} is significantly lower than the one obtained from the mixed window in the most relevant mass range 10^{11} to $10^{14} M_{\odot} h^{-1}$. Therefore the ESP mass function will not describe the numerical results well when the effective window is used. At very least, the prescription has to be modified and/or calibrated with simulation results again. However, we note that this result is hard to modify because large effect comes from the prefactor $(V/V_*)/(\gamma\nu)$, which is independent of the shape of the barrier and the scatter around it.

Although using the mixed window approach does not sound appealing, are we really compelled to use the effective window function? The window function required to fit the cross bias parameter should be the same as that used to compute the moments. Our finding that the effective window is necessary to get a good fit of the cross bias parameter implies that for self-consistency we have to use the effective window function in the prediction as well.

The peak model generally is accurate only in the high peak limit, for example for massive halos. Our finding that the ESP mass function is lower than the numerical results for halos of mass $\lesssim 10^{14} M_{\odot} h^{-1}$ can be interpreted as that only part of the low to medium mass halos can arise from peaks in the primordial field.

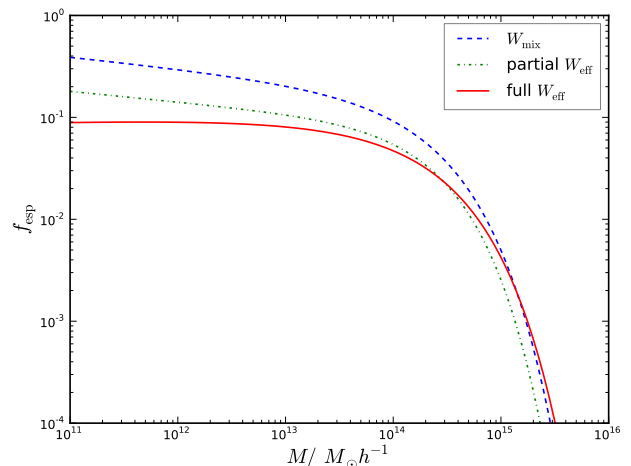


FIG. 6. ESP multiplicity function f_{esp} as a function of mass obtained with different prescriptions: $f_{\text{esp}}^{\text{G}}$ with moments computed using mixed window (dashed, blue), $f_{\text{esp}}^{\text{G}}$ computed using the effective window (dotted-dashed, green), and full f_{esp} with moments obtained with the effective window (solid, red).

V. THE HALO MODEL FOR THE LAGRANGIAN CROSS POWER SPECTRUM

A popular model to describe the dark matter, halo and galaxy correlations is the halo model [33–36]. The

halo profile is an important ingredient of the halo model. In this section, we check if the Lagrangian cross power spectrum can be described in the halo model formalism.

In the halo model, all the matter in the universe is assumed to reside within halos. In particular, both the matter and halo power spectrum are decomposed into the so-called 1-halo term and 2-halo term. In this section we will focus on the cross power spectrum between halo and matter. Following the usual halo model prescription [36], the Lagrangian cross power spectrum between dark matter and halo in the mass range $[m_{h1}, m_{h2}]$ can be expressed as

$$P_c = P_{2h} + P_{1h}, \quad (25)$$

with P_{2h} and P_{1h} given by

$$P_{2h}(k) = P_m(k) \frac{1}{\bar{n}_h} \int_{m_{h1}}^{m_{h2}} d \ln m_h \frac{dn}{d \ln m_h} b_1(m_h, k) \\ \times \int_{m=0}^{m=\infty} d \ln m \frac{m}{\bar{\rho}_m} \frac{dn}{d \ln m} b_1(m, k) W_{\text{eff}}(m, k), \quad (26)$$

$$P_{1h}(k) = \frac{1}{\bar{n}_h} \int_{m_{h1}}^{m_{h2}} d \ln m_h \frac{dn}{d \ln m_h} \frac{m_h}{\bar{\rho}_m} W_{\text{eff}}(m_h, k), \quad (27)$$

where $P_m(k)$ is the linear power spectrum evaluated at the initial time, and $dn/d \ln m$ is the halo mass function. In terms of the mass function, $\bar{\rho}_m$ and \bar{n}_h can be expressed as

$$\bar{\rho}_m = \int_{m=0}^{m=\infty} d \ln m \frac{dn}{d \ln m} m, \quad (28)$$

$$\bar{n}_h = \int_{m_{h1}}^{m_{h2}} d \ln m_h \frac{dn}{d \ln m_h}. \quad (29)$$

The linear bias b_1 denotes

$$b_1(m, k) = 1 + b_{10}(m, k) + 2b_{01}(m, k) \frac{d \ln W_{\text{eff}}(m, k)}{d \ln s_0(m)}, \quad (30)$$

where b_{10} and b_{01} are extrapolated to the initial redshift using the linear growth factor and have used the Eulerian version of the bias parameter. This is in line with the usual halo model formulated in the Eulerian space. In the Appendix C we show the details of the derivation of Eq. 26 and 27.

In the halo model, even though we are interested in halos in a small mass range, we still need to integrate over a large range of mass due to the matter part. To compute the halo model prediction, we use the Sheth-Tormen mass function [37]. Numerically one needs to integrate to very small mass in the 2-halo term to get convergent results. Similarly for the excursion set bias parameters, we have to rely on the analytic formula over a vast range of mass scale that the model has not been tested. In Fig. 7, we compare the halo model results with the numerical measurements using the Lagrangian halos from Carmen at $z = 0$. We have plotted the 1-halo and 2-halo terms.

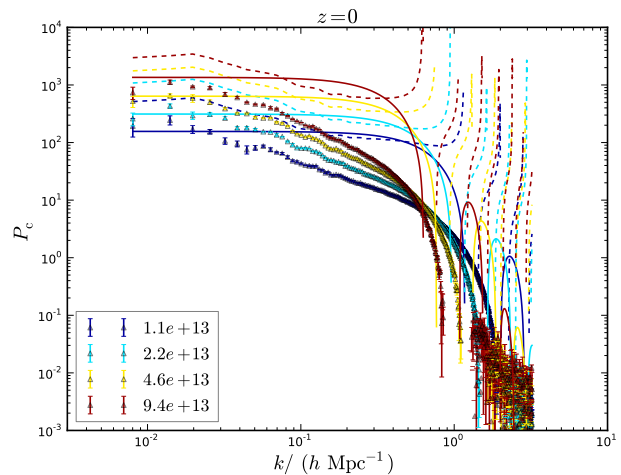


FIG. 7. The Lagrangian cross power spectrum obtained from the halo model is compared with the numerical results (triangular data points). The 1-halo term (solid line) and 2-halo term (dashed line) are plotted respectively. For the same mass, they are shown with the same color. The data are from Carmen simulation at $z = 0$.

The 2-halo term describes the correlation between two different halos. In the 2-halo term, scale-independent linear bias is often used. However, in light of our results in previous sections, we shall use the full scale-dependent bias b_1 . For the linear bias parameters, we shall compute them following [14]. One of the reasons for the success of the Eulerian halo model is that in the low k regime, the matter part integral in Eq. 26

$$P_{2h}^m = \int_{m=0}^{m=\infty} d \ln m \frac{m}{\bar{\rho}_m} \frac{dn}{d \ln m} b_1(m, k) W_{\text{eff}}(m, k) \quad (31)$$

reduces to 1 as W_{eff} approaches 1 as k goes to zero (see Eq. 71 in [36]). This is guaranteed to be true because in the standard halo model, the bias parameters are the peak-background split bias obtained by differentiating the mass function. Thus P_{2h} reduces to $b_1 P_{\text{Lin}}$ in the low k limit as expected. This is not necessarily true in the peak theory as not all the matter is located in peaks, thus there is no reason that P_{2h}^m would reduce to 1 in the low k limit. Indeed we have checked that it does not hold, and the deviation from unity at low k is about 8% at $z = 0$. This relatively small deviation at $z = 0$ is further amplified when we extrapolate the bias factors to $z_* = 49$. As can be seen from Fig. 7, the 2-halo term is larger than the simulation results by a factor of unity at low k .

The 1-halo term describes the correlation between the halo and the matter around the halo. In the standard halo model picture, the 1-halo term is negligible at low k and only starts to dominate for $k \gtrsim 0.5 \text{ Mpc}^{-1} h$. Again, insight can be gained by considering the low k regime, where W_{eff} reduces to 1. In this regime, it is clear that P_{1h} is the same as that in the Eulerian halo

model. However, the magnitude of the Lagrangian cross power spectrum is smaller than its Eulerian counterpart by one power of the growth factor. This means that P_{1h} is relatively much more significant than in the Eulerian case. From Fig. 7, we find that the 1-halo term alone already gives comparable or larger power than the simulation results at low k . We should emphasize that the halo model predicting the shot noise contribution for the cross power spectrum is already a problem in usual halo model, it only gets exacerbated in Lagrangian space.

We find that both the 2-halo and 1-halo terms give large power at low k , and hence the overall power is larger than the simulation results by at least a factor of a few at low k . Thus the halo model would not work naturally in the Lagrangian space without substantial modification being made. Various modifications to the standard halo model have been proposed, some of them include the halo exclusion effects [38, 39] while others combine perturbation theory with halo model [40, 41]. One of the potential improvement is to include the halo exclusion effect in the 2-halo term. In Eq. 26, we have assumed that the halo exclusion effect is negligible. In the Eulerian halo model, the halo size is small, ignoring the exclusion effect may not be a serious problem, while for Lagrangian halos, it is not negligible due to their large sizes. Halo exclusion effect reduces the large scale power, thus it can alleviate the problem that there is too much power at large scales. Among the modifications suggested, the splitting of the matter power spectrum into 1-halo and 2-halo parts proposed in [40] is particularly noteworthy as it is done in the Lagrangian space. The splitting is based on the probability that two particles in the Lagrangian space will fall into the same Lagrangian halo. To calculate this probability one needs p_h , and a top-hat was assumed in [40]; realistically, one would use p_h shown in Fig. 1. This Lagrangian splitting is in fact similar to the exclusion effects in the 2-halo term proposed in the Eulerian halo model, because the probability distribution effectively introduces exclusion for the Lagrangian halos automatically. Another intriguing property of the model proposed in [40] is that there is a counter term in the 1-halo term arising from a trivial Dirac delta function. This counter term cancels the constant part of the halo profile and results in leading k^2 correction only in the 1-halo term. This may reduce the large power of 1-halo term that we found. However, it is not clear that this trivial Dirac delta function already cancels out in the standard halo model formalism. In this section, we have explored the standard halo model, it is beyond the scope of this paper to investigate these possibilities further.

VI. CONCLUSIONS

It is often assumed that the profile of the Lagrangian halos is given by a top hat window function. However, besides being a convenient approximation in the context of the spherical collapse model, there is no fundamental

reason why the Lagrangian halo profile should be of the form of a top hat. In this paper, we study the profile of the Lagrangian halo using numerical simulations.

Top hat assumption is of course an idealization. Realistically, we expect some particles within the Lagrangian patch of the halo with sufficiently high escape velocity will fly out of it, while some will fall in. Thus we expect that the Lagrangian halo profile will be more extended than a top hat. We measure the spherical profile of the Lagrangian halos by stacking halos together. Indeed the Lagrangian halo profile in real space is more extended than a top hat but less diffuse than a Gaussian. In particular, on average there is still a few per cents of the total particles near the center of mass of the Lagrangian halo do not make it into the final Eulerian halos. We find that the Lagrangian halo window function can be modeled by a product of a top hat and a Gaussian in Fourier space. We also find analytic form in real space. Thus the modification needed compared to the usual top hat assumption is little.

In Fourier space, the effective bias parameter obtained from the cross power spectrum contains both bias parameters and the window function. The theories such as the peak model can give precise prediction for the scale-dependent bias. The window function contributes additional scale-dependence although its precise form is not constrained by the theory. To distinguish the scale-dependence due to the bias parameters, the window function must be modeled accurately as well. We find that using the effective window function together with the bias functional form suggested by the excursion set theory, we are able to fit the data well up to $kR_{\text{Lag}} \sim 10$. It is important to note that we find that the same window function is required to fit the Lagrangian halo profile in real space and the cross power spectrum in Fourier space. This is an important self-consistency check.

In models predicting the clustering of the Lagrangian halos, such as the peak model, various spectral moments are required. The top hat window is often used for s_0 , while for higher order moments Gaussian window is used as top hat window will lead to divergent results. However, as we find that the effective window is required to fit the cross bias parameter, we should use the effective window function to compute the moments for self-consistency. The effective window function is more localized in real space than Gaussian, and yet it gives all the convergent spectral moment thanks to its Gaussian component. Thus the effective window offers a unified treatment for all the moments.

We check the ESP mass function when the effective window function is used. We find that the resultant mass function is significantly lower than that from the mixed window approach for halos of mass $\lesssim 10^{14} M_{\odot} h^{-1}$. As previously it was shown that when the mixed window was used, the resultant mass function agrees with simulation results very well, we conclude that when the effective window function is used the results will be significantly lower than the numerical ones. Because the peak model

is generally accurate when the high peak limit applies, such as for the massive halos, we can interpret the deficit of the ESP mass function compared to simulation results as that only part of the low mass halos can arise from peaks.

We also check if the halo model formalism can be used to describe the Lagrangian cross power spectrum. We find that both the 1-halo and 2-halo terms are comparable or larger than the numerical result at low k already. Thus it cannot be applied directly. One of the potential improvement to the present model is to include the halo exclusion effect.

Being armed with an accurate effective window function, we are able to measure the scale-dependent bias parameters accurately. We shall present the details of the measurement of the bias parameters and explore the relations among them [28]. In particular we shall check the so-called consistency relations [14, 31] that these bias parameters should satisfy.

ACKNOWLEDGMENT

We thank LasDamas project ¹ for the simulations used in the work. The simulations were run using a Teragrid allocation and some RPI and NYU computing resources were also used. KCC thanks the hospitality of the ICTP in Trieste and the theory group of CERN, where part of the work was done. KCC acknowledges the support from the Swiss National Science Foundation.

Appendix A: The linking length dependence of the Lagrangian halo profile

In the main text we have presented the results using halos obtained with linking length $b = 0.156$. In this section, we study the linking length dependence of the Lagrangian halo profile by comparing the halo profile obtained with $b = 0.156$ and $b = 0.2$.

In Fig. 8, we compare the Lagrangian halo profiles obtained with the two different linking lengths. In this plot, we have used Lagrangian halos obtained from Carmen simulation at $z = 0$. We have considered a narrow mass group whose mean mass is $9.4 \times 10^{13} M_{\odot} h^{-1}$. We find that with larger b the Lagrangian halo profile becomes more compact. In particular, the fraction of the particles near the halo center that are incorporated into the final Eulerian halos is enhanced when larger b is used. However, one should bear in mind that suppose a halo is identified with $b = 0.156$ to be of certain mass, when $b = 0.2$ is applied, this halo will be classified to be a halo of larger mass. Thus if we compare the halos obtained

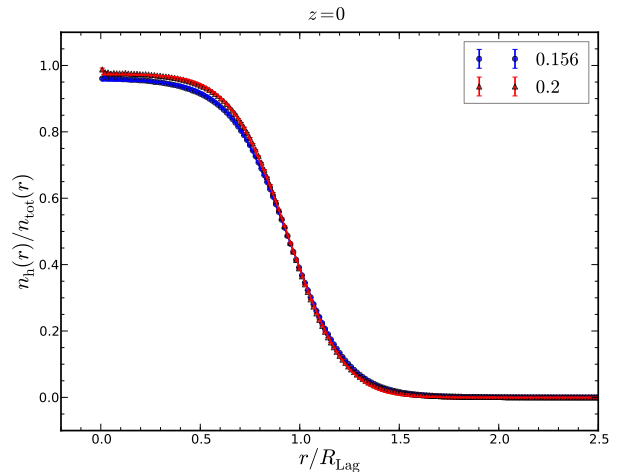


FIG. 8. The Lagrangian halo profile obtained from Eulerian halos with $b = 0.156$ (blue circles) and 0.2 (red triangles) respectively. In this plot, both groups are in the same mass range, whose mean mass is $9.4 \times 10^{13} M_{\odot} h^{-1}$.

with $b = 0.156$ and $b = 0.2$ in a narrow mass range, we are in fact comparing different objects.

We now select the samples such that we are comparing the same halos. To make sure we are comparing the same object, we search the halo catalog in the $b = 0.2$ group and select the ones that match the center of mass positions in the $b = 0.156$ group. For the mass group whose mean mass $9.6 \times 10^{13} M_{\odot} h^{-1}$ in the $b = 0.156$ catalog, we find that the corresponding group in $b = 0.2$ has a mean mass increased by about 20% to $1.1 \times 10^{14} M_{\odot} h^{-1}$. In Fig. 9, we compare the profiles of these two groups. Note that R_{Lag} is computed using the mean mass of the corresponding group. The results are very similar to those in Fig. 8. Increase in b results in a more compact halo group.

Appendix B: The excursion set peak mass function with general window function

Excursion set peak (ESP) mass function was derived in [12–14]. However, Gaussian window is assumed in the derivation in those references. In this section, we shall review the derivation of ESP mass function, but we will also generalize it to the case with general window function. The computations below follow Appendix A of [2] closely.

In peak theory, we are interested in the correlation between the density contrast δ , its spatial derivatives $\eta_i = \partial_i \delta$, and its second derivatives $\zeta_{ij} = \partial_{ij} \delta$. We will also impose the first crossing constraint on the peaks. To do so we need an extra variable μ [12, 13, 42]

$$\mu = \frac{d\delta}{ds_0}. \quad (\text{B1})$$

¹ <http://lss.phy.vanderbilt.edu/lasdamas>

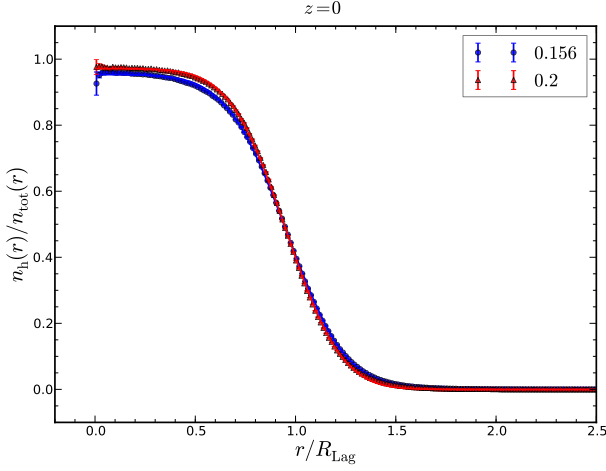


FIG. 9. Similar to Fig. 8 except in this plot, the samples are chosen such that the halos in the $b = 0.156$ group are the same as those in the $b = 0.2$ group. For the $b = 0.156$ group, the mean mass is $9.6 \times 10^{13} M_{\odot} h^{-1}$, while the mean mass of the $b = 0.2$ group is $1.1 \times 10^{14} M_{\odot} h^{-1}$.

We will assume that the field is Gaussian, thus the statistics of the field is fully encoded in the covariance matrix. The field is smoothed with a general window function W , although most of the time we will keep it implicit.

Suppose we assume the vector to be $\mathbf{V} = (\delta, \mu, \zeta_{11}, \zeta_{22}, \zeta_{33}, \zeta_{12}, \zeta_{23}, \zeta_{13}, \eta_1, \eta_2, \eta_3)^T$, then the elements of the covariance matrix $M = \langle \mathbf{V}\mathbf{V}^T \rangle$ are

$$\langle \delta^2 \rangle = s_0, \quad (\text{B2})$$

$$\langle \delta\mu \rangle = \frac{1}{2}, \quad (\text{B3})$$

$$\langle \delta\eta_i \rangle = 0, \quad (\text{B4})$$

$$\langle \delta\zeta_{ij} \rangle = -\frac{1}{3}s_1\delta_{ij}, \quad (\text{B5})$$

$$\langle \mu^2 \rangle = \sigma_{\mu}^2 = \int \frac{d^3k}{(2\pi)^3} P(k) \left(\frac{dW}{ds_0} \right)^2, \quad (\text{B6})$$

$$\langle \mu\eta_i \rangle = 0, \quad (\text{B7})$$

$$\langle \mu\zeta_{ij} \rangle = -\frac{1}{6}\delta_{ij} \frac{ds_1}{ds_0}, \quad (\text{B8})$$

$$\langle \eta_i\eta_j \rangle = \frac{1}{3}s_1\delta_{ij}, \quad (\text{B9})$$

$$\langle \eta_i\zeta_{jk} \rangle = 0, \quad (\text{B10})$$

$$\langle \zeta_{ij}\zeta_{kl} \rangle = \frac{s_2}{15}(\delta_{ij}\delta_{kl} + \delta_{ik}\delta_{jl} + \delta_{il}\delta_{jk}). \quad (\text{B11})$$

The full covariance matrix M is 11-dimensional. Fortunately from Eq. B2-B11, we see that M is block diagonal and the part of M due to $\zeta_{12}, \zeta_{23}, \zeta_{13}, \eta_1, \eta_2$, and η_3 is

simply

$$M_2 = \text{Diag}\left(\frac{s_2}{15}, \frac{s_2}{15}, \frac{s_2}{15}, \frac{s_1}{3}, \frac{s_1}{3}, \frac{s_1}{3}\right). \quad (\text{B12})$$

The Gaussian distribution

$$\begin{aligned} p_G(V_1, \dots, V_{11}) \prod_i dV_i \\ = \frac{1}{\sqrt{(2\pi)^{11} \det M}} \exp\left(-\frac{1}{2}\mathbf{V}^T M^{-1}\mathbf{V}\right) \prod_i dV_i \end{aligned} \quad (\text{B13})$$

is invariant under coordinate transformation, and so we can evaluate it in any convenient coordinate system. Following [2], we can define the variables

$$\sigma_2 x = -(\zeta_{11} + \zeta_{22} + \zeta_{33}), \quad (\text{B14})$$

$$\sigma_2 y = -\frac{1}{2}(\zeta_{11} - \zeta_{33}), \quad (\text{B15})$$

$$\sigma_2 z = -\frac{1}{2}(\zeta_{11} - 2\zeta_{22} + \zeta_{33}). \quad (\text{B16})$$

to diagonalize the correlations between the diagonal elements of ζ_{ij} . In place of δ and μ , we will also use the normalized variables

$$\nu = \frac{\delta}{\sigma_0}, \quad (\text{B17})$$

$$u = \frac{\mu}{\sigma_{\mu}}. \quad (\text{B18})$$

The part of M related to ν, u, x, y , and z can then be written as

$$M_1 = \begin{pmatrix} 1 & \alpha & \gamma & 0 & 0 \\ \alpha & 1 & \beta & 0 & 0 \\ \gamma & \beta & 1 & 0 & 0 \\ 0 & 0 & 0 & \frac{1}{15} & 0 \\ 0 & 0 & 0 & 0 & \frac{1}{5} \end{pmatrix}, \quad (\text{B19})$$

with α and β denote

$$\alpha = \frac{1}{2\sigma_0\sigma_{\mu}}, \quad (\text{B20})$$

$$\beta = \frac{1}{2\sigma_2\sigma_{\mu}} \frac{ds_1}{ds_0}, \quad (\text{B21})$$

$$\gamma = \frac{s_1}{\sigma_0\sigma_2}. \quad (\text{B22})$$

If the window function is Gaussian, then

$$\frac{ds_1}{ds_0} = \frac{s_2}{s_1}, \quad (\text{B23})$$

$$\sigma_{\mu}^2 = \frac{s_2}{4s_1^2}, \quad (\text{B24})$$

and hence α is reduced to γ and β becomes 1. Therefore u and x are perfectly correlated. In this case the joint probability distribution is reduced to [12, 13]

$$P_G(\nu, u, x, y, z) = P_G(\nu, x, y, z) \delta_D(x - u). \quad (\text{B25})$$

However, we will not assume Gaussian window here. In this case, p_G is given by

$$p_G(\nu, u, \zeta_i, \vec{\eta}) \prod dV_i = \frac{1}{\sqrt{(2\pi)^{11} \det M}} e^{-Q} d\nu du d^3\eta \prod_{i=1}^6 d\zeta_i. \quad (\text{B26})$$

We have denoted ζ_{ii} by ζ_i for $i = 1, 2$, and 3 , while ζ_{12} , ζ_{23} and ζ_{31} by ζ_4 , ζ_5 , and ζ_6 respectively. Using Eq. B19 and B12, the quadratic form Q can be expressed as

$$\begin{aligned} Q &= \frac{1}{2} \mathbf{V}^T M^{-1} \mathbf{V} \\ &= \frac{1}{2(1 - \alpha^2 - \beta^2 + \alpha\beta\gamma)} \left[u^2 + (1 - \alpha^2)x^2 + (1 - \beta^2)\nu^2 - (\gamma - 2\alpha\beta)x\nu - (2\beta - \alpha\gamma)ux - (2\alpha - \beta\gamma)u\nu \right] \\ &\quad + \frac{15}{2}y^2 + \frac{5}{2}z^2 + \frac{15}{2s_2}(\zeta_4^2 + \zeta_5^2 + \zeta_6^2) + \frac{3}{2s_1}\vec{\eta} \cdot \vec{\eta}. \end{aligned} \quad (\text{B27})$$

The volume element for a 3×3 symmetric matrix can be written in term of the eigenvalues in the principle frame [2]

$$\prod_{i=1}^6 d\zeta_i = |(\lambda_1 - \lambda_2)(\lambda_2 - \lambda_3)(\lambda_3 - \lambda_1)| d\lambda_1 d\lambda_2 d\lambda_3 dV(SO(3)), \quad (\text{B28})$$

where λ_i is the eigenvalue in the principle frame and we assume that the eigenvalues are ordered such that

$$\lambda_1 \geq \lambda_2 \geq \lambda_3. \quad (\text{B29})$$

In the principle frame, x , y and z are defined by Eq. B14-B16 with ζ_{ii} replaced by λ_i . $dV(SO(3))$ is the volume elements of the $SO(3)$ group. The probability distribution is independent of it. We will integrate over it and we will get a factor of $2\pi^2$.

Using Eq. B28 and B14-B16, we get

$$d\nu du d^3\eta \prod_{i=1}^6 d\zeta_i \frac{1}{\sqrt{\det M}} = d\nu du d^3\eta 2\sigma_2^3 |y(z^2 - y^2)| dx dy dz \frac{1}{\sqrt{\det M_1 \det M_2}}. \quad (\text{B30})$$

Note that the Jacobian determinant $|\partial(\lambda_1, \lambda_2, \lambda_3)/\partial(x, y, z)|$ from the measure and $\det M$ cancels each other. From Eq. B19 and B12, we have

$$\det M_1 \det M_2 = \frac{(1 - \alpha^2 - \beta^2 + \alpha\beta\gamma)s_1^3 s_2^3}{9 \times 15^5}. \quad (\text{B31})$$

and hence

$$d\nu du d^3\eta \int_{S_3} \prod_{i=1}^6 d\zeta_i \frac{1}{(2\pi)^{11/2} \sqrt{\det M}} = \frac{3 \times 15^{5/2}}{(2\pi)^{7/2} \sqrt{1 - \alpha^2 - \beta^2 + \alpha\beta\gamma}} |y(z^2 - y^2)| d\nu du dx dy dz \frac{d^3\eta}{\sigma_1^3}. \quad (\text{B32})$$

The number density of peaks can be obtained by the Kac-Rice formula [2]

$$\begin{aligned} n_{\text{pk}}(\mathbf{r}) &= |\det \zeta_{ij}| \Theta(\lambda_3) \delta_D(\vec{\eta}(\mathbf{r})) \\ &= \frac{\sigma_2^3}{3^3} |(2z - x)[(z + x)^2 - (3y)^2]| \Theta(\lambda_3) \delta_D(\vec{\eta}(\mathbf{r})), \end{aligned} \quad (\text{B33})$$

where the constraint $\delta_D(\vec{\eta}(\mathbf{r}))$ selects the extremum points and $\lambda_3 > 0$ ensures that the extrema are peaks.

We can obtain the mean differential number density by averaging over the joint Gaussian distribution as

$$\begin{aligned} \mathcal{N}_{\text{pk}}(\nu, u, x, y, z) &= d\nu du |2\sigma_2^3 y(z^2 - y^2)| dx dy dz \int d^3\eta P_G(\nu, u, x, y, z, \vec{\eta}) \frac{\sigma_2^3}{3^3} |(2z - x)[(z + x)^2 - (3y)^2]| \Theta(\lambda_3) \delta_D(\vec{\eta}) \\ &= \frac{5^{5/2} \sqrt{3}}{(2\pi)^{7/2} \sqrt{1 - \alpha^2 - \beta^2 + \alpha\beta\gamma}} \frac{\sigma_2^3}{\sigma_1^3} |y(z^2 - y^2)(2z - x)[(z + x)^2 - (3y)^2]| e^{-\tilde{Q}} \chi d\nu du dx dy dz, \end{aligned} \quad (\text{B34})$$

where χ is the indicator function, which is 1 when the integration variables are in the specified domain, zero otherwise and \tilde{Q} denotes

$$\begin{aligned}\tilde{Q} &= \frac{1}{2} \mathbf{x}^T M^{-1} \mathbf{x} \\ &= \frac{1}{2(1 - \alpha^2 - \beta^2 + \alpha\beta\gamma)} \left[u^2 + (1 - \alpha^2)x^2 + (1 - \beta^2)\nu^2 - (\gamma - 2\alpha\beta)x\nu - (2\beta - \alpha\gamma)ux - (2\alpha - \beta\gamma)u\nu \right] \\ &\quad + \frac{15}{2}y^2 + \frac{5}{2}z^2.\end{aligned}\tag{B35}$$

The ESP number density can be obtained by imposing the first-crossing constraint on the peak number density as [12, 13, 42]

$$\begin{aligned}\mathcal{N}_{\text{esp}}(s_0, u, x, y, z) \Delta s_0 du dx dy dz \\ = \frac{5^{5/2} \sqrt{3}}{(2\pi)^{7/2} \sqrt{1 - \alpha^2 - \beta^2 + \alpha\beta\gamma}} \frac{\sigma_2^3}{\sigma_1^3} du dx dy dz \int_{\nu_c}^{\nu_c + \mu \frac{\Delta s_0}{\sigma_0}} d\nu |y(z^2 - y^2)(2z - x)[(z + x)^2 - (3y)^2]| e^{-\tilde{Q}} \chi.\end{aligned}\tag{B36}$$

It essentially ensures that the smoothed δ upcrosses the barrier by the condition that

$$\delta(s) > \delta_c, \quad \delta(s - \Delta s) < \delta_c,\tag{B37}$$

which translates to

$$\delta_c < \delta(s) < \delta_c + \mu \Delta s.\tag{B38}$$

The upcrossing condition also requires μ to be positive.

For small Δs_0 , we can reduce the ν -integral to

$$\begin{aligned}\mathcal{N}_{\text{esp}}(s_0, u, x, y, z) \Delta s_0 du dx dy dz \\ = \frac{5^{5/2} \sqrt{3}}{(2\pi)^{7/2} \sqrt{1 - \alpha^2 - \beta^2 + \alpha\beta\gamma}} \frac{\sigma_2^3}{\sigma_1^3} \frac{\sigma_\mu \Delta s_0}{\sigma_0} du dx dy dz u |y(z^2 - y^2)(2z - x)[(z + x)^2 - (3y)^2]| e^{-\tilde{Q}(\nu_c)} \chi.\end{aligned}\tag{B39}$$

Note that \tilde{Q} now is evaluated at $\nu = \nu_c$.

As u only couples to x and ν_c , we can integrate over z and y as in [2]. The ESP number density in the interval Δs_0 is given by

$$\mathcal{N}_{\text{esp}}(s_0) \Delta s_0 = \frac{1}{(2\pi)^2} \left(\frac{\sigma_2}{\sqrt{3}\sigma_1} \right)^3 \frac{\sigma_\mu \Delta s_0}{\sigma_0} e^{-\frac{\nu_c^2}{2}} E(\nu_c, \alpha, \beta, \gamma),\tag{B40}$$

where E is defined as

$$E(\nu, \alpha, \beta, \gamma) = \int_0^\infty dx \int_0^\infty du u f(x) \frac{1}{\sqrt{(2\pi)^2 (1 - \alpha^2 - \beta^2 + \alpha\beta\gamma)}} e^{-B},\tag{B41}$$

with B given by

$$\begin{aligned}B(\nu, x, u; \alpha, \beta, \gamma) &= \frac{1}{2(1 - \alpha^2 - \beta^2 + \alpha\beta\gamma)} \left[\alpha(\alpha - \beta\gamma)\nu^2 + u^2 + (1 - \alpha^2)x^2 \right. \\ &\quad \left. - (\gamma - 2\alpha\beta)x\nu - (2\beta - \alpha\gamma)ux - (2\alpha - \beta\gamma)u\nu \right].\end{aligned}\tag{B42}$$

The function $f(x)$ is given by [2]

$$f(x) = \frac{x^3 - 3x}{2} \left\{ \text{erf} \left[\sqrt{\frac{5}{2}} x \right] + \text{erf} \left[\sqrt{\frac{5}{2}} \frac{x}{2} \right] \right\} + \sqrt{\frac{2}{5\pi}} \left[\left(\frac{31x^2}{4} + \frac{8}{5} \right) e^{-\frac{5x^2}{8}} + \left(\frac{x^2}{2} - \frac{8}{5} \right) e^{-\frac{5x^2}{4}} \right].\tag{B43}$$

Using $\nu \mathcal{N}(\nu) = 2s \mathcal{N}(s)$, we arrive at

$$\mathcal{N}_{\text{esp}}(\nu_c) = \frac{1}{(2\pi)^2} \left(\frac{\sigma_2}{\sqrt{3}\sigma_1} \right)^3 \frac{1}{\nu_c \alpha} e^{-\frac{\nu_c^2}{2}} E(\nu_c, \alpha, \beta, \gamma).\tag{B44}$$

Therefore f_{esp} is given by

$$f_{\text{esp}}(\nu_c) = \frac{M}{\rho_m} \mathcal{N}_{\text{esp}}(\nu_c) = \frac{V}{V_*} \frac{e^{-\frac{\nu_c^2}{2}}}{\sqrt{2\pi}} \frac{1}{\nu_c \alpha} E(\nu_c, \alpha, \beta, \gamma). \quad (\text{B45})$$

To facilitate the comparison with [13], we have defined two volumes

$$V = \frac{M}{\rho_m}, \quad V_* = (6\pi)^{\frac{3}{2}} \left(\frac{\sigma_1}{\sigma_2} \right)^3. \quad (\text{B46})$$

When Gaussian window is used, α reduces to γ , and hence the prefactor is the same as that in [13], and E can be regarded as a generalization of G_1 in [13].

Now we further generalize the ESP mass function to the moving barrier case. The first crossing condition is modified to

$$\delta(s) > B(s), \quad \delta(s - \Delta s) < B(s - \Delta s), \quad (\text{B47})$$

which means

$$B(s) < \delta(s) < B(s) + [\mu - B'(s)]\Delta s. \quad (\text{B48})$$

To upcross the barrier, the minimal u is modified to

$$u_0 = \frac{B'(s)}{\sigma_\mu}. \quad (\text{B49})$$

This effectively modifies the integration limits of ν and u integrals, and the end results is that E -integral is modified to

$$E(\nu, \alpha, \beta, \gamma) = \int_0^\infty dx f(x) \int_{u_0}^\infty du (u - u_0) \frac{e^{-B}}{\sqrt{(2\pi)^2(1 - \alpha^2 - \beta^2 + \alpha\beta\gamma)}}. \quad (\text{B50})$$

Appendix C: Cross power spectrum in the halo model

In this section, we derive the cross power spectrum between dark matter and halo. Here we follow the usual halo model prescription [36]. In the halo model, all the dark matter is assumed to reside within halos. For halos, we only consider the distribution of the center of mass of the halos, while for matter we also keep track of the halo profile as it represents the distribution of matter.

The number density of halos is given by

$$n_h(\mathbf{x}) = \sum_i^{\text{sub}} \delta_D(\mathbf{x} - \mathbf{x}_i), \quad (\text{C1})$$

where \mathbf{x}_i represents the center of mass of the halos and ‘‘sub’’ means that the sum is over a subset of halos in certain mass range $[m_{h1}, m_{h2}]$. The mean number density of halos is

$$\bar{n}_h(\mathbf{x}) = \left\langle \sum_i^{\text{sub}} \delta_D(\mathbf{x} - \mathbf{x}_i) \right\rangle = \int_{m_{h1}}^{m_{h2}} d \ln m \frac{dn}{d \ln m}. \quad (\text{C2})$$

Similarly we can write the matter density distribution

as

$$\rho_m(\mathbf{x}) = \sum_i^{\text{all}} m_i W(\mathbf{x} - \mathbf{x}_i), \quad (\text{C3})$$

where W is window function representing the profile of the halo and m_i is the mass of the i^{th} halo. We use ‘‘all’’ to emphasize that for dark matter we need to sum over all the halos. Alternatively, we can write ρ_m as

$$\rho_m(\mathbf{x}) = \int d^3 x' \int_0^\infty dm m \delta_D(\mathbf{x} - \mathbf{x}') \times \sum_i^{\text{all}} \delta_D(m - m_i) \delta_D(\mathbf{x}' - \mathbf{x}_i). \quad (\text{C4})$$

The advantage of this form is that we can isolate the stochastic variables in the Dirac delta functions. The mean matter density is then given by

$$\bar{\rho}_m = \int_{m=0}^{m=\infty} d \ln m m \frac{dn}{d \ln m}. \quad (\text{C5})$$

The cross correlation function can be expressed as

$$\langle \delta_m(\mathbf{x}_1) \delta_h(\mathbf{x}_2) \rangle = \frac{1}{\bar{\rho}_m \bar{n}_h} \langle \rho_m(\mathbf{x}_1) n_h(\mathbf{x}_2) \rangle - 1. \quad (\text{C6})$$

We can use Eq. C1 and C4 to compute the correlator $\langle \rho_m(\mathbf{x}_1)n_h(\mathbf{x}_2) \rangle$. There are two types of terms, correlation in the same halo (1-halo term) and among two different halos (2-halo term).

For the 1-halo term, we sum over the overlapping halos in ρ_m and n_h as

$$\begin{aligned} & \xi_{1h}(\mathbf{x}_1 - \mathbf{x}_2) \\ &= \frac{1}{\bar{\rho}_m \bar{n}_h} \int d^3x' d^3x'' \int_0^\infty dm m W(\mathbf{x}_1 - \mathbf{x}') \delta_D(\mathbf{x}_2 - \mathbf{x}'') \\ & \quad \times \left\langle \sum_i^{\text{sub}} \delta_D(m - m_i) \delta_D(\mathbf{x}' - \mathbf{x}_i) \delta_D(\mathbf{x}'' - \mathbf{x}_i) \right\rangle \\ &= \frac{1}{\bar{\rho}_m \bar{n}_h} \int d^3x' d^3x'' \int_{m_{h1}}^{m_{h2}} dm_h m_h W(\mathbf{x}_1 - \mathbf{x}') \delta_D(\mathbf{x}_2 - \mathbf{x}'') \\ & \quad \times \delta_D(\mathbf{x}' - \mathbf{x}'') \frac{dn}{dm_h} \\ &= \frac{1}{\bar{n}_h} \int_{m=m_{h1}}^{m=m_{h2}} d \ln m_h \frac{dn}{d \ln m_h} \frac{m_h}{\bar{\rho}_m} W(\mathbf{x}_1 - \mathbf{x}_2). \end{aligned} \quad (\text{C7})$$

In Fourier space, it becomes Eq. 27.

We now go to the 2-halo term, which is obtained by summing over different halos

$$\begin{aligned} & \frac{1}{\bar{\rho}_m \bar{n}_h} \int d^3x' d^3x'' \int_0^\infty dm m W(\mathbf{x}_1 - \mathbf{x}') \delta_D(\mathbf{x}_2 - \mathbf{x}'') \\ & \left\langle \sum_{\substack{i \in \text{all}, j \in \text{sub} \\ i \neq j}} \delta_D(m - m_i) \delta_D(\mathbf{x}' - \mathbf{x}_i) \delta_D(\mathbf{x}'' - \mathbf{x}_j) \right\rangle. \end{aligned} \quad (\text{C8})$$

The term in the angular bracket can be written as

$$\frac{dn}{dm} \int_{m_{h1}}^{m_{h2}} dm_h \frac{dn}{dm_h} [1 + \xi_{hh}(\mathbf{x}' - \mathbf{x}'')]. \quad (\text{C9})$$

Note that the unity in the square bracket in Eq. C9 will give unity after the integrations, and hence it will cancel the unity in Eq. C6. Thus the 2-halo term is given by

$$\begin{aligned} & \xi_{2h}(\mathbf{x}_1 - \mathbf{x}_2) \\ &= \frac{1}{\bar{\rho}_m \bar{n}_h} \int d^3x' d^3x'' \int_0^\infty dm m W(\mathbf{x}_1 - \mathbf{x}') \delta_D(\mathbf{x}_2 - \mathbf{x}'') \\ & \quad \times \int_{m_{h1}}^{m_{h2}} dm_h \frac{dn}{dm} \frac{dn}{dm_h} \xi_{hh}(\mathbf{x}' - \mathbf{x}''). \end{aligned} \quad (\text{C10})$$

It becomes Eq. 26 in Fourier space after replacing $P_{hh}(k)$ by $b_1(m, k)b_1(m_h, k)P(k)$. This replacement implicitly ignores the halo exclusion effect. This seems to be a good approximation for Eulerian halo model, however the halo exclusion effect can be significant for Lagrangian halos due to their large sizes. As we discuss in the main text, straightforward application of the halo model yields too much power at large scales. On the other hand, the halo exclusion effect reduces the power at large scales. These point to the need to properly include the exclusion effect for Lagrangian halos in the halo model. However, this is beyond the scope of this paper.

-
- [1] J. R. Bond, S. Cole, G. Efstathiou, and N. Kaiser, *ApJ* **379**, 440 (1991).
- [2] J. M. Bardeen, J. R. Bond, N. Kaiser, and A. S. Szalay, *ApJ* **304**, 15 (1986).
- [3] J. R. Bond and S. T. Myers, *ApJS* **103**, 1 (1996).
- [4] V. Desjacques, *Phys. Rev. D* **78**, 103503 (2008), arXiv:0806.0007.
- [5] V. Desjacques and R. K. Sheth, *Phys. Rev. D* **81**, 023526 (2010), arXiv:0909.4544.
- [6] V. Desjacques, M. Crocce, R. Scoccimarro, and R. K. Sheth, *Phys. Rev. D* **82**, 103529 (2010), arXiv:1009.3449.
- [7] V. Desjacques, *Phys. Rev. D* **87**, 043505 (2012), arXiv:1211.4128.
- [8] J. E. Gunn and J. R. Gott, III, *ApJ* **176**, 1 (1972).
- [9] P. J. E. Peebles, *The Large-Scale Structure of the Universe* (Princeton University Press, New Jersey, 1980).
- [10] T. Padmanabhan, *Structure formation in the Universe* (Cambridge University Press, Cambridge, 1993).
- [11] D. Lynden-Bell, *MNRAS* **136**, 101 (1967).
- [12] L. Appel and B. J. T. Jones, *MNRAS* **245**, 522 (1990).
- [13] A. Paranjape and R. K. Sheth, *MNRAS* **426**, 2789 (2012).
- [14] A. Paranjape, R. K. Sheth, and V. Desjacques, *MNRAS* **431**, 1503 (2013), arXiv:1210.1483.
- [15] M. Biagetti, K. C. Chan, V. Desjacques, and A. Paranjape, *MNRAS* **441**, 1457 (2014).
- [16] A. Paranjape, E. Sefusatti, K. C. Chan, V. Desjacques, P. Monaco, and R. K. Sheth, *MNRAS* **436**, 449 (2013).
- [17] C. Porciani, A. Dekel, and Y. Hoffman, *MNRAS* **332**, 339 (2002).
- [18] A. Elia, A. D. Ludlow, and C. Porciani, *MNRAS* **421**, 3472 (2012).
- [19] G. Despali, G. Tormen, and R. K. Sheth, *MNRAS* **431**, 1143 (2013).
- [20] T. Baldauf, V. Desjacques, and U. Seljak, (2014), arXiv:1405.5885.
- [21] K. C. Chan, (2015), arXiv:1507.04753.
- [22] N. Dalal, M. White, J. R. Bond, and A. Shirokov, *ApJ* **687**, 12 (2008).
- [23] T. Baldauf, in *Perturbative approaches to redshift space distortions workshop, Zurich* (2012).
- [24] U. Seljak and M. Zaldarriaga, *ApJ* **469**, 437 (1996), arXiv:astro-ph/9603033.
- [25] M. Crocce, S. Pueblas, and R. Scoccimarro, *MNRAS* **373**, 369 (2006), arXiv:astro-ph/0606505.
- [26] V. Springel, *MNRAS* **364**, 1105 (2005), arXiv:astro-ph/0505010.
- [27] M. Davis, G. Efstathiou, C. S. Frenk, and S. D. M. White, *ApJ* **292**, 371 (1985).
- [28] K. C. Chan, R. K. Sheth, and R. Scoccimarro, in preparation (2015).
- [29] N. Frusciante and R. K. Sheth, *JCAP* **1211**, 016 (2012), arXiv:1208.0229.
- [30] K. C. Chan, R. Scoccimarro, and R. K. Sheth, *Phys. Rev. D* **85**, 083509 (2012), arXiv:1201.3614.
- [31] M. Musso, A. Paranjape, and R. K. Sheth, *MNRAS* **427**,

- 3145 (2012).
- [32] B. E. Robertson, A. V. Kravtsov, J. Tinker, and A. R. Zentner, *ApJ* **696**, 636 (2009).
- [33] U. Seljak, *MNRAS* **318**, 203 (2000).
- [34] J. A. Peacock and R. E. Smith, *MNRAS* **318**, 1144 (2000).
- [35] R. Scoccimarro, R. K. Sheth, L. Hui, and B. Jain, *ApJ* **546**, 20 (2001).
- [36] A. Cooray and R. Sheth, *Phys. Rep.* **372**, 1 (2002), arXiv:astro-ph/0206508.
- [37] R. K. Sheth, H. J. Mo, and G. Tormen, *MNRAS* **323**, 1 (2001).
- [38] R. E. Smith, R. Scoccimarro, and R. K. Sheth, *Phys. Rev. D* **75**, 063512 (2007), arXiv:astro-ph/0609547.
- [39] R. E. Smith, V. Desjacques, and L. Marian, *Phys. Rev. D* **83**, 043526 (2011), arXiv:1009.5085.
- [40] P. Valageas and T. Nishimichi, *A&A* **527**, 26 (2011), arXiv:1009.0597.
- [41] I. Mohammed and U. Seljak, *MNRAS* **445**, 3382 (2014), arXiv:1407.0060.
- [42] M. Musso and R. K. Sheth, *MNRAS* **423**, 102 (2012).